A second radio flare from the tidal disruption event AT2020vwl: a delayed outflow ejection?

Goodwin, A.J.; Mummery, A.; Laskar, T.; Alexander, K.D.; Anderson, G.E.; Bietenholz, M.; ... ; Velzen, S. van

The Astrophysical Journal, 981:122 (15pp), 2025 March 10 https://doi.org/10.3847/1538-4357/adb0b1

A Second Radio Flare from the Tidal Disruption Event AT2020vwl: A Delayed Outflow Ejection?

A. J. Goodwin[1], A. Mummery[2], T. Laskar[3], K. D. Alexander[4], G. E. Anderson[1], M. Bietenholz[5], C. Bonnerot[6,7], C. T. Christy[4], W. Golay[8,9], W. Lu[10,11], R. Margutti[11,12], J. C. A. Miller-Jones[1], E. Ramirez-Ruiz[13], R. Saxton[14], and S. van Velzen[15]

[1] International Centre for Radio Astronomy Research—Curtin University, GPO Box U1987, Perth, WA 6845, Australia
[2] Oxford Theoretical Physics, Beecroft Building, Clarendon Laboratory, Parks Road, Oxford, OX1 3PU, UK
[3] Department of Physics & Astronomy, University of Utah, Salt Lake City, UT 84112, USA
[4] Department of Astronomy/Steward Observatory, 933 North Cherry Avenue, Rm. N204, Tucson, AZ 85721-0065, USA
[5] SARAO/Hartebeesthoek Radio Observatory, PO Box 443, Krugersdorp 1740, South Africa
[6] School of Physics and Astronomy, University of Birmingham, Birmingham, B15 2TT, UK
[7] Institute for Gravitational Wave Astronomy, University of Birmingham, Birmingham, B15 2TT, UK
[8] Center for Astrophysics—Harvard & Smithsonian, 60 Garden St., Cambridge, MA 02138, USA
[9] Department of Astrophysics/IMAPP, Radboud University, P.O. Box 9010, 6500 GL, Nijmegen, The Netherlands
[10] Departments of Astronomy, University of California, Berkeley, CA 94720, USA
[11] Theoretical Astrophysics Center, University of California, Berkeley, CA 94720-3411, USA
[12] Department of Physics, University of California, Berkeley, CA 94720, USA
[13] Department of Astronomy and Astrophysics, University of California, Santa Cruz, CA 95064, USA
[14] Telespazio UK for ESA, European Space Astronomy Centre, Operations Department, 28691 Villanueva de la Canada, Spain
[15] Leiden Observatory, Leiden University, Postbus 9513, 2300 RA Leiden, The Netherlands
Received 2024 October 22; revised 2025 January 24; accepted 2025 January 27; published 2025 March 4

Abstract

We present the discovery of a second radio flare from the tidal disruption event (TDE) AT2020vwl via long-term monitoring radio observations. Late-time radio flares from TDEs are being discovered more commonly, with many TDEs showing radio emission thousands of days after the stellar disruption, but the mechanism that powers these late-time flares is uncertain. Here, we present radio spectral observations of the first and second radio flares observed from the TDE AT2020vwl. Through detailed radio spectral monitoring, we find evidence for two distinct outflow ejection episodes or a period of renewed energy injection into the preexisting outflow. We deduce that the second radio flare is powered by an outflow that is initially slower than the first flare but carries more energy and shows tentative indication of accelerating over time. Through modelling the long-term optical and UV emission from the TDE as arising from an accretion disk, we infer that the second radio outflow launch or energy injection episode occurred approximately at the time of the peak accretion rate. The fast decay of the second flare precludes environmental changes as an explanation, while the velocity of the outflow is at all times too low to be explained by an off-axis relativistic jet. Future observations that search for any link between the accretion disk properties and late-time radio flares from TDEs will aid understanding of what powers the radio outflows in TDEs and confirm if multiple outflow ejections or energy injection episodes are common.

Unified Astronomy Thesaurus concepts: Tidal disruption (1696); Radio transient sources (2008); Black hole physics (159); High energy astrophysics (739)

Materials only available in the online version of record: machine-readable table

1. Introduction

A tidal disruption event (TDE) occurs when a star in the center of a galaxy passes too close to the supermassive black hole (SMBH) and is destroyed (e.g., M. J. Rees 1988). TDEs produce bright flares observed across the electromagnetic spectrum (e.g., K. Auchettl et al. 2017; K. D. Alexander et al. 2020; S. van Velzen et al. 2020), providing a unique opportunity to witness the real-time evolution of accretion onto a previously dormant SMBH. During a TDE, approximately half of the stellar debris remains on bound orbits, to eventually be accreted by the SMBH, while the other half is unbound (M. J. Rees 1988) and can be ejected at significant velocities.

In recent years, dozens of new TDEs have been discovered, primarily via transient emission in the optical, UV, or soft X-ray (e.g., S. van Velzen et al. 2020). In the optical and UV, TDEs are characterized by a 1–2 mag rise in the optical flux of the nucleus of a quiescent galaxy (although TDEs can occur in active galaxies, they are more difficult to classify), followed by a longer decay that approximately follows the theoretical fallback rate onto an SMBH, $L \propto t^{-5/3}$ (where L is the bolometric luminosity and t is time; e.g., E. S. Phinney 1989; B. Mockler et al. 2019; S. van Velzen et al. 2021; E. Hammerstein et al. 2023; Y. Yao et al. 2023). Optical spectral observations of TDEs usually show transient broad H and/or He lines (see, e.g., Y. Yao et al. 2023 for a recent study) and can show blueshifted emission lines interpreted as signatures of outflowing material (e.g., M. Nicholl et al. 2020). The optical/UV emission from TDEs is well described by thermal blackbody emission with a temperature of $\sim 10^4$ K (e.g., S. Gezari et al. 2009; J. Guillochon et al. 2014; S. van Velzen et al. 2020). Simulations of TDEs have shown that

the optical/UV emission may be powered by an accretion disk that forms rapidly after the disruption (e.g., J. Guillochon et al. 2014; H. Shiokawa et al. 2015; C. Bonnerot et al. 2016; K. Hayasaki et al. 2016; A. Mummery & S. A. Balbus 2020), debris collisions and shocks (e.g., L. Dai et al. 2015; W. Lu & C. Bonnerot 2020), or an envelope of debris that reprocesses higher-energy emission from closer to the SMBH (e.g., A. Loeb & A. Ulmer 1997; B. D. Metzger & N. C. Stone 2016; N. Roth et al. 2016; B. D. Metzger 2022).

Long-term optical monitoring of TDEs has revealed a flattening and excess of optical emission present in approximately two-thirds of optical light curves years post the initial flare (A. Mummery et al. 2024b). These late-time optical plateaus are well modeled by emission from an accretion disk with continued accretion onto the SMBH at significantly sub-Eddington rates (A. Mummery et al. 2024b). Long-term optical monitoring of TDEs has also revealed a handful of events that show unusual late-time behavior, including ones that rebrighten (e.g., J. J. Somalwar et al. 2023; Y. Yao et al. 2023), interpreted as being due to a partial disruption of the star.

X-ray emission from TDEs is less uniform. Some show thermal X-ray emission that tends to decay within months of the optical flare (e.g., M. Guolo et al. 2024), although not all events produce detectable X-ray emission. Others show bright nonthermal X-ray emission associated with a relativistic jet (e.g., J. S. Bloom et al. 2011; D. N. Burrows et al. 2011; A. J. Levan et al. 2011; B. A. Zauderer et al. 2011; I. Andreoni et al. 2022; D. R. Pasham et al. 2023). Others again show rebrightening or rapid variability in the X-rays (e.g., A. Malyali et al. 2024), which in some cases has also been interpreted as being due to partial disruption of the star (e.g., Z. Liu et al. 2023, 2024; A. Malyali et al. 2023) or accretion disk changes (L. L. Thomsen et al. 2022).

Radio observations of TDEs probe synchrotron emission from electrons that are accelerated in the shocks formed from outflows and jets. It has been proposed that outflows and jets from TDEs are launched by accretion-induced winds or magnetic-field-induced ejections from the disk (e.g., S. van Velzen et al. 2016), debris collisions (e.g., A. J. Goodwin et al. 2022), or the unbound debris stream interacting with the circumnuclear medium (CNM; e.g., J. Krolik et al. 2016). However, radio detections of TDEs are uncommon, with <30 TDEs having published radio detections (e.g., K. D. Alexander et al. 2020), and only a handful have been monitored continuously from the onset of the outflow (e.g., A. J. Goodwin et al. 2022). Very rarely ($\sim$1% of observed events), a TDE produces a highly collimated, relativistic, radio-emitting jet (J. S. Bloom et al. 2011; D. N. Burrows et al. 2011; A. J. Levan et al. 2011; B. A. Zauderer et al. 2011; I. Andreoni et al. 2022; D. R. Pasham et al. 2023), while others present slower-moving, likely less collimated, radio-emitting outflows (e.g., K. D. Alexander et al. 2016; Y. Cendes et al. 2021; R. Stein et al. 2021; C. T. Christy et al. 2024; A. J. Goodwin et al. 2024).

TDEs show diverse radio properties and the origin of these differences is not well understood. Recent radio observations have complicated the theoretical interpretation of the radio emission from TDEs by illuminating that at least 40% show late-time ($\gtrsim$500 days) radio flaring, apparently not associated with optical or X-ray reflares (A. Horesh et al. 2021a; Y. Cendes et al. 2023; A. Anumarlapudi et al. 2024). The source of these late-time flares is currently being hotly debated by the community, with the leading scenarios being a delayed radio jet or renewed energy injection from accretion (e.g., Y. Cendes et al. 2023), an off-axis jet coming into view (e.g., T. Matsumoto & T. Piran 2023), or new interactions with inhomogeneous clouds in the CNM (T. Matsumoto & T. Piran 2024; J. Zhuang et al. 2024). To date, most TDEs that show late-time ($\gtrsim$500 days) rising radio emission do not have comprehensive radio observations at early times, making it difficult to determine if the late-time radio emission is linked to outflows produced at the time of the initial stellar disruption and if it is a rebrightening of a radio flare at earlier times.

The TDE AT2020vwl (also Gaia20etp or ZTF20achpcvt) was discovered on 2020 October 10 by the Gaia spacecraft as a $\sim$1 mag optical flare at the center of the galaxy SDSS J153037.80+265856.8/LEDA 1794348 at a distance of 147 Mpc (J2000 R.A., decl. 15:30:37.800, +26:58:56.89; S. T. Hodgkin et al. 2020). The event was also observed by the Zwicky Transient Facility (ZTF; Y. Yao et al. 2023) and classified by E. Hammerstein et al. (2021) as a TDE, based on the optical spectral properties, bright UV flux, and optical light curve. A prompt radio-emitting outflow was observed at the time of the event and attributed to an outflow likely produced during the circularization of the stellar debris in the first tens of days post disruption (A. J. Goodwin et al. 2023).

In this work, we present long-term radio observations of the TDE AT2020vwl, spanning 97–1220 days post optical flare. Our observations reveal a second radio flare beginning approximately 400 days after the optical flare began, in addition to the first radio flare reported by A. J. Goodwin et al. (2023). These observations track the evolution of both the first and second radio flares, providing a unique opportunity in this work to constrain the mechanism of the late-time rising radio emission in this source.

The paper is laid out as follows: in Section 2, we describe the new radio observations and data reduction processes; in Section 3, we present and model the radio light curve at different frequencies; in Section 4, we model the radio spectra and physical outflow properties; in Section 5, we present the disk model fits to the multiwavelength light curves of the event; in Section 6, we discuss the implications of the outflow and disk constraints, including possible explanations for the second radio flare; and, finally, in Section 7, we provide a summary of the results.

2. Observations

We observed AT2020vwl on multiple occasions with the Karl G. Jansky Very Large Array (VLA), the upgraded Giant Metrewave Radio Telescope (uGMRT), and the MeerKAT radio telescope, between 2022 November 1 and 2024 March 26, at various frequencies in the range 0.6–16.6 GHz. In addition A. J. Goodwin et al. (2023) reported seven epochs of radio observations between 2021 February 3 and 2022 May 8, which we also include in our analysis. A summary of the new radio observations and measured flux densities of AT2020vwl is provided in Appendix A in Table 3.

2.1. VLA

We observed the coordinates of AT2020vwl on five occasions with the VLA, between 2022 November 1 and 2024 March 26, at 1–16.6 GHz. All data were reduced using the same method as in A. J. Goodwin et al. (2023), with calibration and imaging performed in the Common Astronomy

Software Application (CASA, version 5.6.3; J. P. McMullin et al. 2007; CASA Team et al. 2022), using standard procedures including the VLA calibration pipeline (version 5.6.3). Flux and bandpass calibration was done with 3C 286 in all observations. Observations were carried out at a central frequency of 1.5 GHz (*L* band) with 1 GHz of bandwidth, 3 GHz (*S* band) with 2 GHz of bandwidth, 6 GHz (*C* band) with 4 GHz of bandwidth, 10 GHz (*X* band) with 4 GHz of bandwidth, and 15 GHz (*Ku* band) with 6 GHz of bandwidth. 8-bit samplers were used for the *L* and *S* bands, and 3-bit samplers were used for the *Ku*, *X*, and *C* bands. For phase calibration, we used ICRF J151340.1+233835 for 2–18 GHz (the *Ku*, *X*, *C*, and *S* bands) and ICRF J160207.2+332653 for 1–2 GHz (the *L* band). The flux density of the target was extracted in the image plane using imfit, by fitting an elliptical Gaussian fixed to the synthesized beam.

2.2. uGMRT

We observed AT2020vwl with the uGMRT on four occasions between 2023 April and 2023 November. The observations were taken in band 4, with a central frequency of 0.65 GHz and total bandwidth of 300 MHz, and band 5, with a central frequency of 1.26 GHz and total bandwidth of 400 MHz. Each observing band was broken into 2048 spectral channels. Data reduction was carried out using the same procedures as in A. J. Goodwin et al. (2023), including standard procedures in CASA (version 5.6.3). Flux and bandpass calibration were done with 3C 286 and phase calibration with ICRF J160207.2+332653. The flux density of the target was again extracted in the image plane using imfit, by fitting an elliptical Gaussian fixed to the synthesized beam. Unfortunately the band 5 observation taken in 2023 April suffered from issues with the flux calibration scan, resulting in poor flux calibration of the data. We therefore do not include this observation in our analysis.

2.3. MeerKAT

We observed AT2020vwl with the South African MeerKAT radio telescope on 2024 February 27 at a central frequency of 0.8 GHz. We used the 4K (4096-channel) wideband continuum mode with an observed bandwidth from 544 to 1088 MHz, with a central frequency of 816 MHz. The data were reduced using the same procedures as outlined in A. J. Goodwin et al. (2023), including the OxKAT scripts (I. Heywood 2020). We used ICRF J133108.2+303032 (3C 286) and ICRF J193925.0-634245 to set the flux density scale and calibrate the bandpass and ICRF J160913.3+264129 (QSO B1607+268) as a secondary calibrator. The flux density of AT2020vwl was determined by fitting an elliptical Gaussian of the same dimensions as the restoring beam.

2.4. Neil Gehrels Swift Observatory

The Neil Gehrels Swift Observatory (Swift; N. Gehrels et al. 2004) observed AT2020vwl 28 times between 2020 January 7 and 2023 June 27. A. J. Goodwin et al. (2023) reported no X-ray detection of the event in the first 27 observations. We examined the 28th Swift/X-Ray Telescope (XRT) observation taken on 2023 June 27 using the online Swift product builder (P. A. Evans et al. 2009). Again, there was no X-ray source detected at the position of AT2020vwl, with a 3σ upper limit on the 0.3–10 keV unabsorbed X-ray flux $F_X < 3.1 \times 10^{-13}$ erg cm^{-2} s^{-1}, assuming a Galactic hydrogen column density of $N_H = 4.3 \times 10^{20}$ cm^{-2} (R. Willingale et al. 2013) and photon index $\Gamma = 1.5$, as appropriate for TDE X-ray emission (e.g., K. Auchettl et al. 2017; M. Guolo et al. 2024).

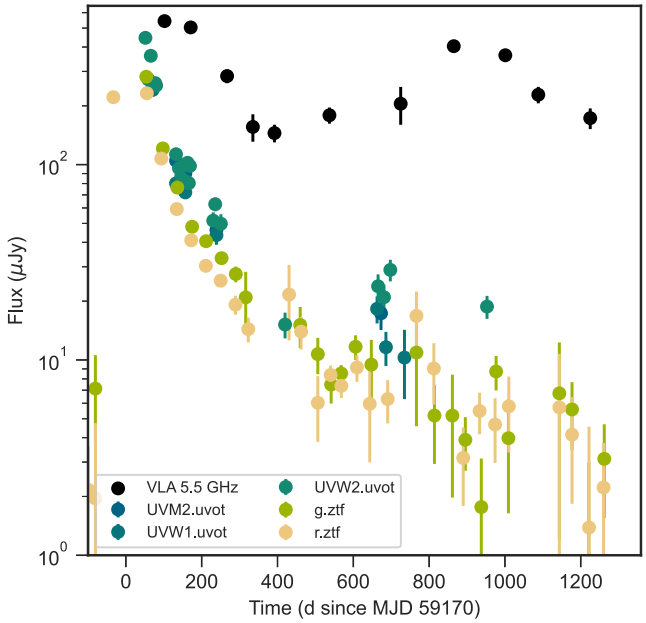

Figure 1. The optical (ZTF *g*- and *r*-band), UV (Swift UVOT), and 5.5 GHz radio (VLA) light curves of AT2020vwl. The optical and UV fluxes have been host-subtracted. The second radio flare does not appear to be correlated with any significant renewed optical or UV activity.

2.5. Interstellar Scintillation

Variability in the radio emission of a compact extragalactic radio source may be induced by interstellar scintillation (ISS; M. A. Walker 1998). A. J. Goodwin et al. (2023) included an additional uncertainty on the observed radio flux densities at all frequencies to account for possible variation in the radio flux density of the compact source induced by ISS. As discussed by A. J. Goodwin et al. (2023), for the Galactic coordinates of AT2020vwl, the radio emission from a compact source will be in the strong, refractive regime until the source reaches an angular size of 134 μs ($\sim 10^{17}$ cm at the distance of AT2020vwl). At source sizes greater than this, we do not expect ISS to cause significant variability in the radio measurements. Since the minimum radio source size is estimated to be largely $<10^{17}$ cm in all new observations presented in this paper, we conservatively include an additional frequency-dependent uncertainty for the spectral modeling. As in A. J. Goodwin et al. (2023), these additional uncertainties on the observed flux density range from 40% at 1.5 GHz to 2% at 18 GHz.

3. Light-curve Fitting

The optical, UV, and 5.5 GHz radio light curves of AT2020vwl are shown in Figure 1. The optical flare began at approximately MJD 59130 (A. J. Goodwin et al. 2023), and radio observations did not begin until 142 days later, at which time fading radio emission was detected.

In the first 400 days post optical flare, the radio emission from AT2020vwl decayed in a frequency-dependent manner, with the decay occurring at higher frequencies first, as reported

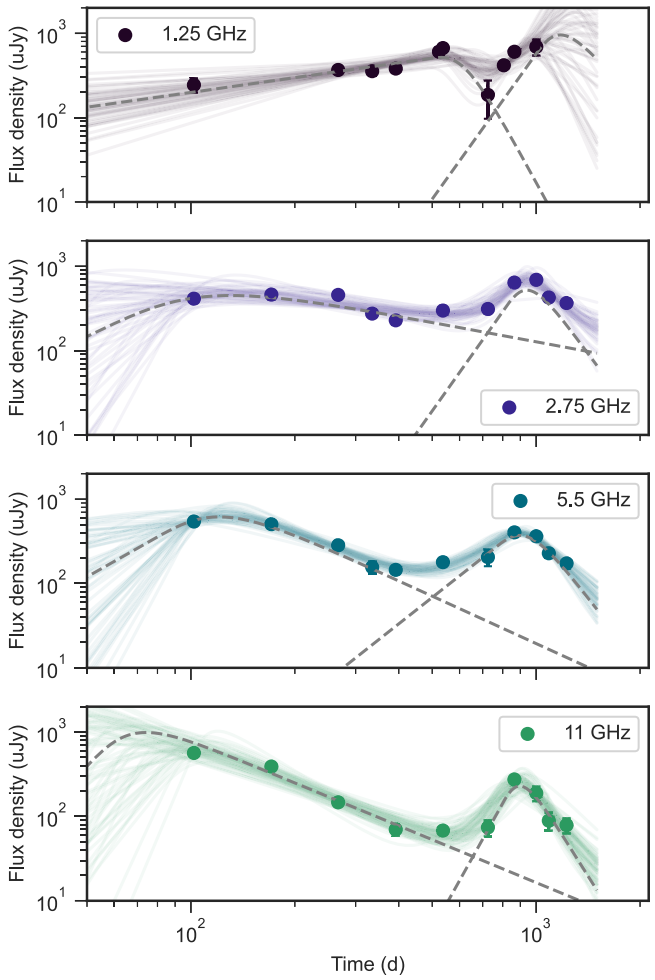

Figure 2. The 1.25, 2.75, 5.5, and 11 GHz observed light curves of AT2020vwl (scatter points) and the two-component broken-power-law fit at each frequency (solid lines). In each panel, 100 random draws from the MCMC posterior distribution are plotted to indicate the uncertainty on the fit. The dashed gray lines show the individual power-law components for the first and second flares, demonstrating that the radio emission from the first power-law component is almost negligible during the second flare, except at the lowest observing frequency of 1.25 GHz.

by A. J. Goodwin et al. (2023). However, between 400 and 600 days post optical flare, our new radio observations reveal that the radio emission began rising at all observed frequencies (Figure 2). The radio emission rose quickly (over 100–200 days) and began decaying at frequencies >2 GHz between 800 and 900 days post optical flare.

In order to constrain the rate of rise and decay of the radio emission at the different observed frequencies, we fit the individual frequency light curves with a broken-power-law model. Following the R. A. Chevalier (1998) prescription for modeling the time evolution of a self-absorbed synchrotron source, we assume the observed flux density at each frequency, F_ν, is described by

$$F_\nu = 1.582 F_{\nu,tc}\left(\frac{t}{t_c}\right)^a\left[1-\exp\left(-\left(\frac{t}{t_c}\right)^{-(a+b)}\right)\right], \quad (1)$$

where F_ν is the flux density at frequency ν, $F_{\nu,tc}$ is the flux density at the break time t_c, and a and b are the power-law slope either side of the break time, where each observed frequency has different t_c, a, and b. In order to model the two radio flares, we assume two broken power laws, such that

$$F_{\nu,\mathrm{total}} = F_{\nu,1} + F_{\nu,2}, \quad (2)$$

where $F_{\nu,1}$ and $F_{\nu,2}$ (and the associated $t_{c,1}$, $t_{c,2}$, etc.) are each given by Equation (1).

We use a Markov Chain Monte Carlo (MCMC) approach to fit Equation (2) to the radio light curves at the observed frequencies of 1.25, 2.75, 5.5, and 11 GHz. We use the Python implementation of MCMC, `emcee` (D. Foreman-Mackey et al. 2013), and flat prior distributions on all modeled parameters, where we allow the parameters to vary between: $0.1 < \log F_{\nu,tc}\,(\mu\mathrm{Jy}) < 6$; $0 < a < 10$; $0 < b < 10$; and $400 < t_c\,(\mathrm{day}) < 1500$. We run each chain with 200 walkers for 3000 steps, conservatively discarding the first 2000 steps for burn-in. We note that for the light-curve fitting, we do not subtract a host component from the observations, as we do for the spectral fitting in Section 4.1, because the host component is constant at each frequency, very small compared to the observed flux densities, and would introduce an additional systematic error as it cannot be well constrained until the transient emission no longer dominates the observed radio emission.

Using this approach, we constrain the peak times of each of the two flares at each frequency, as well as the power-law indices of the rising and decaying portions of the light curves. We note that the rise of the first radio flare is not as well constrained as the second flare, because the radio observations did not begin until 142 days post optical flare. The values of the fitted light-curve parameters are listed in Table 1, and the corresponding best-fit light curves are plotted in Figure 2.

The light-curve fits indicate significantly different properties for the first and second radio flares. Both radio flares peaked earliest at higher frequencies, with a difference of ≈50 days between the 11 GHz peak time and the 2.75 GHz peak time for both the first and second flares. The first flare rose with a temporal power-law index between 1 and 4.4 across all frequencies, while the second flare rose with a temporal power-law index between 3.5 and 7.5, across all frequencies. The first flare decayed with a temporal power-law index between 0.5 and 3, while the second flare decayed with a temporal power-law index between 4 and 6.5. From these light-curve fits, it is clear that the second flare rose and decayed significantly more quickly at all frequencies than the first flare, but the delay between the peak times at the observed frequencies was similar.

4. Spectral Fitting and Outflow Modeling

4.1. Spectral Fits

Next, we examined the radio spectra at each epoch of observations, in order to constrain the evolution of the physical properties of the synchrotron-emitting region. We fit 11 epochs of observed radio spectra, using the same approach as outlined in A. J. Goodwin et al. (2023), including subtracting a host component then fitting the J. Granot & R. Sari (2002) synchrotron spectral model. The exact equations used to fit the synchrotron flux density and constrain the synchrotron peak flux density, F_p, minimum frequency, ν_m, peak frequency, ν_p, and synchrotron energy index, p, are given in Equations (2)–(4) of A. J. Goodwin et al. (2023). We assume that the synchrotron emission is in the regime where $\nu_m < \nu_a < \nu_c$, where ν_c is the synchrotron cooling frequency. We use the same MCMC fitting procedure, using the Python implementation of MCMC,

Table 1
Fitted Light-curve Parameters Using the Two-component Broken-power-law Model Given in Equation (2)

Freq. (GHz)	$F_{\nu,1}$ (μJy)	$t_{c,1}$ (day)	a_1	b_1	$F_{\nu,2}$ (μJy)	$t_{c,2}$ (day)	a_2	b_2
1.25	368^{+68}_{-54}	628^{+63}_{-41}	$0.6^{+0.2}_{-0.2}$	$7.6^{+1.8}_{-3.9}$	>955	>1183	$5.7^{+2.9}_{-2.2}$[a]	$4.6^{+3.7}_{-3.2}$[a]
2.75	433^{+164}_{-106}	120^{+158}_{-68}	$1.6^{+4.4}_{-1.3}$	$0.8^{+1.3}_{-0.4}$	529^{+113}_{-122}	958^{+101}_{-68}	$5.7^{+2.9}_{-3.2}$[a]	$5.4^{+2.4}_{-2.3}$[a]
5.5	606^{+131}_{-179}	127^{+69}_{-22}	$2.1^{+4.0}_{-2.0}$	$1.9^{+0.9}_{-0.5}$	351^{+30}_{-42}	961^{+45}_{-52}	$3.1^{+1.4}_{-0.8}$	$5.4^{+1.5}_{-1.2}$
11	890^{+1767}_{-338}	75^{+39}_{-41}	$4.0^{+3.8}_{-3.0}$	$1.7^{+0.5}_{-0.3}$	225^{+52}_{-48}	907^{+45}_{-48}	$7.2^{+2.0}_{-2.8}$	$6.6^{+1.9}_{-2.0}$

Notes. The uncertainties correspond to the 67% confidence intervals.
[a] The parameter is unconstrained by the MCMC fit and consistent with returning the prior range.

`emcee` (D. Foreman-Mackey et al. 2013). A. J. Goodwin et al. (2023, Appendix A1) explored different synchrotron regimes, including if the peak of synchrotron emission is associated with ν_m instead of ν_a. They found that the spectral fit in which the synchrotron emission is in the regime where $\nu_m < \nu_a$ is statistically significantly preferred. Unlike in A. J. Goodwin et al. (2023), we do not fit for both ν_m and ν_a for the new epochs presented in this work (2022 November 1 and onward), as ν_m has likely shifted below the observed frequencies. Instead, we fit for a single spectral break that we associate with ν_a. The equation used to describe the synchrotron flux is given by J. Granot & R. Sari (2002), i.e.,

$$F_{\nu,\mathrm{synch}} = F_{\nu,\mathrm{ext}}\left[\left(\frac{\nu}{\nu_\mathrm{a}}\right)^{-s\beta_1} + \left(\frac{\nu}{\nu_\mathrm{a}}\right)^{-s\beta_2}\right]^{-1/s}, \quad (3)$$

where ν is the frequency, $F_{\nu,\mathrm{ext}}$ is the normalization, $s = 1.25 - 0.18p$, $\beta_1 = \frac{5}{2}$, and $\beta_2 = \frac{1-p}{2}$.

We use the same prior distributions as in A. J. Goodwin et al. (2023) on all modeled parameters, except notably we decreased the lower bound on the peak frequency to be 0.1 GHz instead of 1 GHz, as the peak frequency in the latest observations is significantly lower than in the earlier epochs. The best-fit synchrotron spectra for each epoch are plotted in Figure 3, and the constrained parameters are listed in Table 4.

The peak flux density and associated peak frequency of the modeled synchrotron spectra are plotted in Figure 4. The peak flux density was initially decreasing following $F_p \propto t^{-2}$, consistent with expectations for synchrotron emission from a nonrelativistic shock propagating in an environment with steep density stratification (Appendix C), until between 400 and 500 days after the onset of the optical flare, at which time it began increasing following $F_p \propto t^1$. The frequency of the peak was initially decreasing, consistent with an expanding synchrotron-emitting region, until ≈500 days post optical flare, at which time it increased for ≈300 days, before beginning to decrease again.

4.2. Outflow Model

In order to constrain the evolution of the physical outflow properties, we model the synchrotron emission as a blastwave that accelerates ambient electrons into a power-law distribution, $N \propto \gamma^{-p}$, where p is the synchrotron energy index and γ is the electron Lorentz factor. We use the same method as outlined in A. J. Goodwin et al. (2023), using the R. Barniol Duran et al. (2013) formalism and Equations (4)–(13) in A. J. Goodwin et al. (2022) to estimate key physical quantities, such as the outflow radius (R), outflow energy (E), magnetic field strength (B), mass of the emitting region (m_ej), ambient electron density (n_e), and velocity of the ejecta (β). We first estimate the equipartition radius (R_eq) and equipartition energy (E_eq), then apply a correction to account for any deviation from equipartition. In this work, we assume the fraction of the total energy in the electrons is 10% and the fraction of the total energy in the magnetic field is 2%, but note that changes in the values of these fractions can cause significant changes in the derived physical outflow quantities, as described in detail by A. J. Goodwin et al. (2023). However, the overall trends in the evolution of the physical outflow quantities remain the same for different assumptions about the deviation from equipartition, as long as these deviations are time-independent. We provide

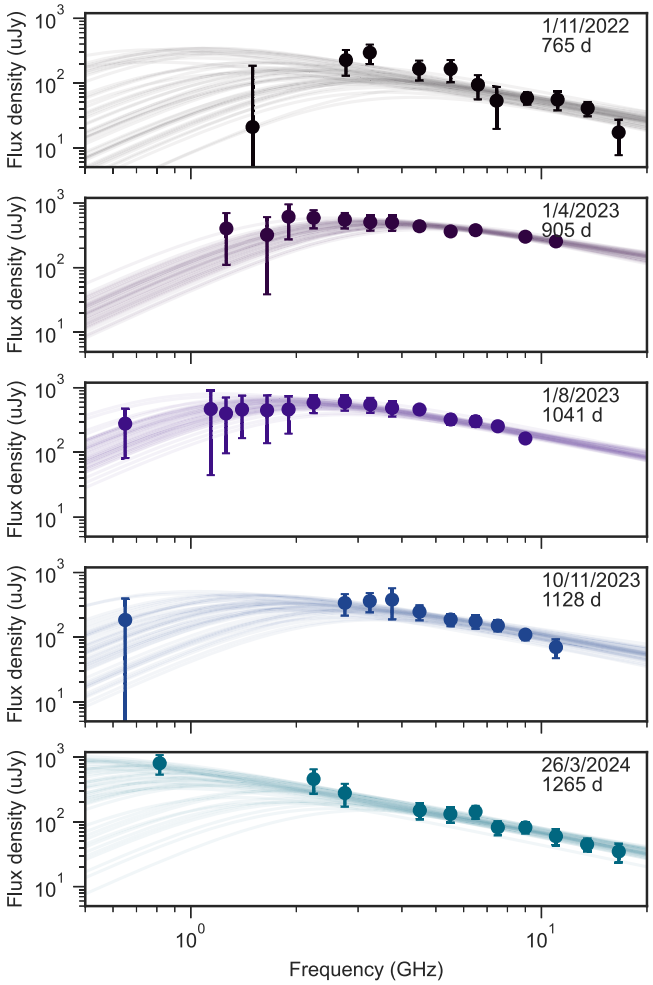

Figure 3. The observed (points) and modeled (lines) synchrotron spectra for AT2020vwl. Each panel is labeled with the UTC date of the observation, and 100 random samples from the MCMC posterior are plotted to indicate the uncertainty in the fits.

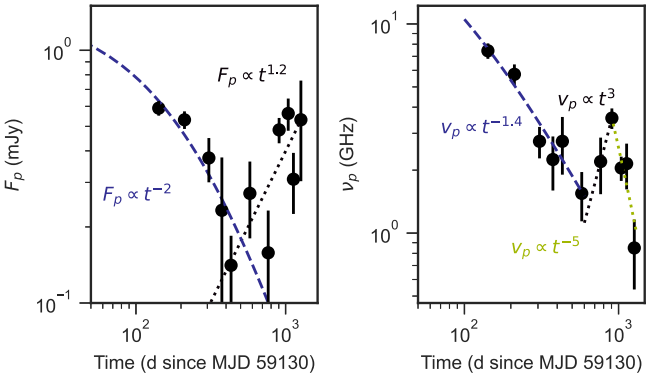

Figure 4. The modeled peak flux density (left) and peak frequency (right) of the synchrotron spectrum of AT2020vwl at each observed radio epoch. The peak flux density and frequency were initially decreasing during the first flare, but began increasing at the onset of the second flare (between 400 and 500 days). The dotted and dashed lines show power-law fits to the rises and decays of the two parameters.

outflow properties for two different geometries: a spherical emitting region and a conical emitting region corresponding to a mildly collimated jet with a half-opening angle of 30°. The exact geometric factors that describe the geometry are the same as in A. J. Goodwin et al. (2023).

The outflow properties we infer are plotted in Figure 5 and listed in Appendix B in Table 4. From the outflow model, we infer the following:

1. It appears that the energy in the outflow was initially constant, until the second flare began, at which time the energy began increasing.
2. The velocity of the outflow was initially constant, until approximately the onset of the rise of the second flare, at which time it decreased by a factor of ∼2, then remained constant until the final epoch, where a tentative increase in the velocity is observed.
3. The ambient density, while less well constrained, initially was decreasing rather steeply with radius, until the second flare, at which time it plateaued for a period before decreasing in the final epoch.
4. The apparent radius of the outflow was initially increasing, and shows a drop or plateau at the time of the second flare, before continuing to increase again.
5. The magnetic field strength, while poorly constrained, is consistent with being constant or decreasing across the course of the observations.
6. The mass in the emitting region increased until the peak of the second flare, after which time it remained approximately constant or decreased slightly.

In Figure 5, it is evident that most of the constrained outflow parameters show a significant change from the initial trends at the time when the second radio flare began dominating the radio emission. This could be evidence of two distinct synchrotron-emitting regions that dominate the radio emission at different epochs. A drop in the radius of the outflow would imply the outflow either had to move inward or the radio emission is dominated by a second, more compact emitting region at this epoch. Noting the large uncertainty on the estimated radius, if we assume two synchrotron-emitting regions, we can fit the radius over time with a linear fit for the first flare (up to 720 days post optical flare) and the second flare (after 720 days post optical flare). We find for two independent synchrotron-emitting sources that the first was launched approximately at the time of optical discovery, while the second was launched between 160 and 700 days after the optical discovery, where the range is determined due to differences in the assumed geometry of the outflow, accounting for uncertainties on the constraints from both geometries and fitting including or excluding the final data point, which is significantly higher than the rest of the data points. We note that these linear fits to the radius are overall poor fits to the data when the final data point is included, pointing toward the variable velocity of the outflow. As an additional caveat, we also note that excluding the data point at 765 days, which may be affected by both emitting regions in the two-outflow scenario, results in an increase in the outflow launch time. In an alternate scenario, a plateau in the radius may be attributed to the initial deceleration of the outflow. Until, at the time of the second flare, renewed energy injection into the outflow causes the velocity to increase and the radius expands at a faster rate. The significantly increasing energy carried by the outflow, evident in Figure 5, beginning at the time of the second flare, is consistent with this scenario. Both of these scenarios require delayed energy injection hundreds of days after the TDE began.

5. Disk Model

In common with most TDEs, the optical and UV light curves of AT2020vwl show a plateau at late times (Figure 6), consistent with direct emission from an accretion flow. In this section, we model this evolving accretion disk using the `FitTeD` code developed by A. Mummery et al. (2024a). The `FitTeD` code uses the A. Mummery (2023) solutions of the relativistic disk evolution equations (S. A. Balbus 2017) to compute multiband light curves, which we fit to the AT2020vwl optical/UV and X-ray data. We take the optical/UV data from the public `manyTDE` repository (A. Mummery et al. 2024b). At optical/UV frequencies, we include both a phenomenological power-law-decay model and a Gaussian rise model, to constrain the early (nondisk) emission. We also include the Swift X-ray upper limits.

The key free parameters of the disk model are: the black hole mass $M_\bullet$ and (dimensionless) spin $a_\bullet$, the initial disk mass $M_{\rm disk}$, the viscous timescale $t_{\rm visc}$, and the disk formation radius r_0 and time t_0. The axis of the disk is inclined by an angle i to the line of sight, also a fitting parameter. These parameters are inferred using standard MCMC techniques (D. Foreman-Mackey et al. 2013). The Markov Chain converged and we found a best-fitting black hole mass of $\log_{10} M_\bullet/M_\odot = 6.55^{+0.3}_{-0.5}$, broadly consistent with galactic scaling relationships: $\log_{10} M_\bullet/M_\odot = 5.6 \pm 0.4$ (scaling with galaxy velocity dispersion; Y. Yao et al. 2023) and $\log_{10} M_\bullet/M_\odot = 6.5 \pm 0.8$ (scaling with galaxy mass; A. Mummery et al. 2024b). The constrained disk parameters are listed in Table 2. Note that the black hole spin parameter and the disk–observer inclination are poorly constrained, owing to the lack of X-ray detections. This is physical; the spin and inclination more strongly affect observations probing the inner disk (X-ray) than outer disk (optical/UV), so these parameters cannot be well constrained for a source such as AT2020vwl, which only has X-ray nondetections.

In the left panel of Figure 6, the model luminosity evolution of the accretion disk in the optical, UV, and X-ray observing bands is plotted along with the observed luminosities and X-ray upper limits. In the right panel, we also show the inferred time evolution of the accretion rate across the innermost stable circular orbit (ISCO) from the model posteriors. AT2020vwl

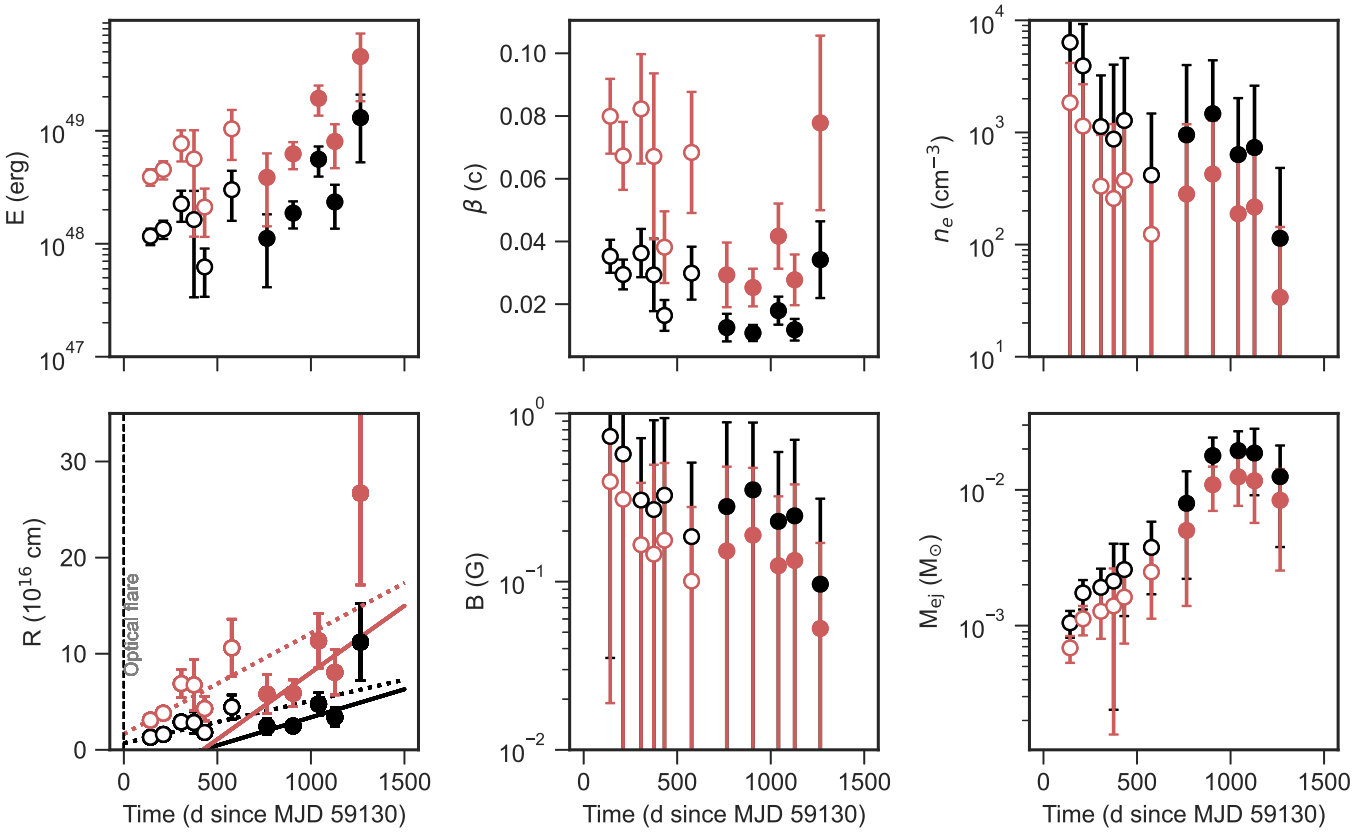

Figure 5. The outflow properties of AT2020vwl. The black points indicate outflow properties for a spherical geometry and the red points are for a conical geometry. The open circles indicate data published in A. J. Goodwin et al. (2023), corresponding to the first radio flare. The closed circles indicate new data presented in this work, corresponding to the second radio flare. In the bottom left panel, the dashed lines indicate linear fits to the radius for the first flare, and the solid lines indicate linear fits to the radius for the second flare.

was never detected in X-rays, and the optical/UV emission at late times is near time independent, so the late-time ISCO accretion rate inferred by the model is poorly constrained. The X-ray upper limits do however provide a strong constraint on the peak of the accretion rate reached in the AT2020vwl system, under the assumption that the X-rays are not obscured. Interestingly, we find the plausible launching time of the second radio outflow ($\Delta t \simeq 160-700$ days post peak), or renewed energy injection, approximately coincides with the time that the peak accretion rate was reached in the system.

6. Discussion

6.1. Did the Outflow Encounter a Denser Region of the CNM?

It has been proposed that radio reflaring events may be explained by a preexisting outflow encountering a denser CNM that can re-accelerate the population of emitting electrons and produce a brightening in the radio emission. Denser clumps in the CNM may be due to an inhomogenous CNM (e.g., A. J. Goodwin et al. 2022), an increase in ambient density at the Bondi radius of the SMBH (e.g., T. Matsumoto & T. Piran 2024), or one or more molecular clouds within the central region of the galaxy (e.g., J. Zhuang et al. 2024).

In other types of synchrotron-emitting transients, such as supernovae and gamma-ray bursts (GRBs) from supernovae, radio light curves occasionally reveal reflares or bumps (M. C. Stroh et al. 2021). These reflares or bumps may be attributed to changes in the circumstellar environment (e.g., SN 2007bg and SN 2014C; P. Salas et al. 2013; G. E. Anderson et al. 2017) or renewed energy injection episodes (e.g., GRB 210726A; G. Schroeder et al. 2024). While the ejection mechanism and environment for supernova outflows are significantly different from those of TDEs, the underlying physics of the synchrotron emission processes remain the same. In the case of changes in the circumstellar environments of supernovae, transitions to denser environments can cause an increase in the radio flux density, as the outflow experiences a stronger shock (P. Salas et al. 2013), and can result in spectral changes of the radio emission.

T. Matsumoto & T. Piran (2024) proposed that the late-time radio flares observed in many TDEs may be explained by the outflow ejected at the time of the stellar disruption encountering the Bondi radius of the SMBH, at which time the CNM density gradient is expected to transition from being relatively steep to approximately flat. T. Matsumoto & T. Piran (2024) point out that for a CNM density profile of $n \propto R^{-k}$, the optically thin synchrotron luminosity, $\nu L_{\nu,\rm thin}$, evolves with time as

$$(\nu L_\nu)_{\rm thin} \propto t^{\frac{12-k(p+5)}{4}} \quad (4)$$

and the optically thick synchrotron luminosity evolves with time as

$$(\nu L_\nu)_{\rm thick} \propto t^{\frac{k+8}{4}}. \quad (5)$$

Taking $p \approx 3$ for AT2020vwl (Table 4), we therefore expect the optically thin radio emission (at the beginning of the rise of the second flare, the radio emission from AT2020vwl was optically thin at frequencies >1 GHz) to evolve as

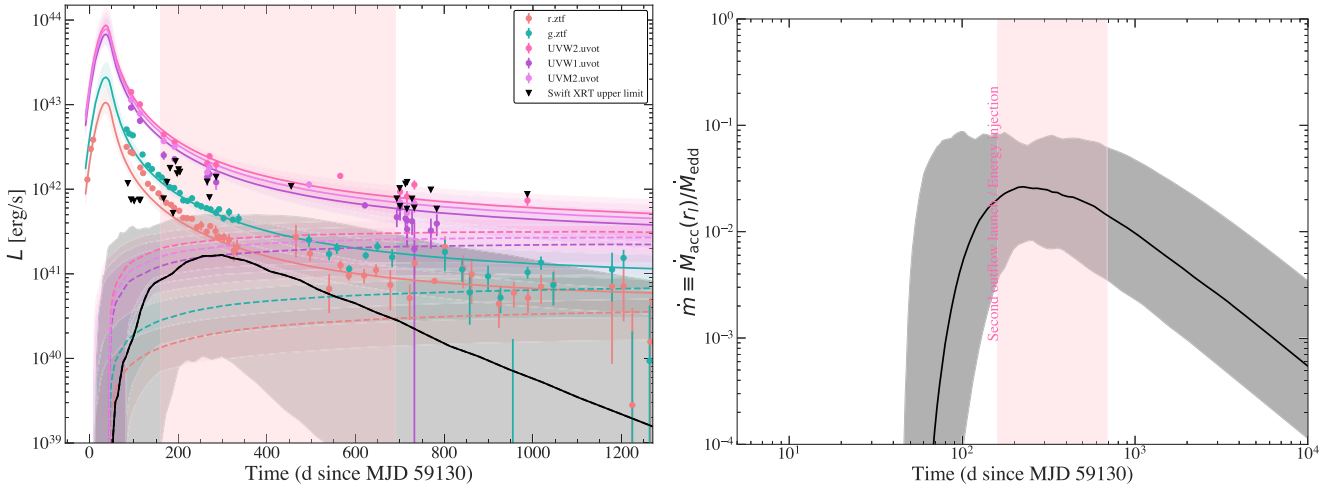

Figure 6. Left: model fits to the observed optical (red and green), UV (pink), and X-ray (black) light curves of AT2020vwl. The solid lines indicate the best-fit model (Gaussian rise + power-law decay + disk), with the shaded regions indicating the 68% credible intervals, and the dashed colored lines show the contributions to the total luminosity from the disk model alone. The inverted triangles indicate 3σ upper limits. Right: the inferred time evolution of the accretion rate across the ISCO from the model posteriors (solid line) and the 68% credible interval (gray shading). The pink shaded region shows the approximate launch time of the second outflow, or the period at which energy injection is required, constrained via the synchrotron radius/energy measurements in Section 4. The energy injection time is approximately coincident with the peak accretion rate reached in the disk model.

Table 2
Modeled Disk Parameters for AT2020vwl

$\log_{10} M_\bullet/M_\odot$	$6.55^{+0.3}_{-0.5}$
$a_\bullet$	$-0.17^{+0.4}_{-0.5}$[a]
$M_{\rm disk}$ ($M_\odot$)	$0.014^{+0.022}_{-0.008}$
r_0 ($GM_\bullet\ c^{-2}$)	40^{+50}_{-20}
$t_{\rm visc}$ (day)	833^{+122}_{-300}
t_0 (day)	6.63^{+82}_{-62}
i (deg)	55^{+26}_{-36}[a]

Notes. The uncertainties correspond to the 67% confidence intervals.
[a] The parameter is unconstrained by the MCMC fit and consistent with returning the prior range.

$(\nu L_\nu)_{\rm thin} \propto t^{-1}$ for $k = 2$ or $(\nu L_\nu)_{\rm thin} \propto t^{-2}$ for $k = 2.5$. At the Bondi radius, T. Matsumoto & T. Piran (2024) propose the density gradient may change to $k = 0$, which would result in the optically thin radio emission transitioning to evolve as $(\nu L_\nu)_{\rm thin} \propto t^3$. Indeed, as found by A. J. Goodwin et al. (2023), the initial decay of the radio light curves at all frequencies is well described by an optically thin synchrotron-emitting source with $k = 2$–2.5 and $p = 3$ (Table 1). However, the second flare was observed to rise with $(\nu L_\nu)_{\rm thin} \propto t^{3.5}$ to $t^{7.5}$, significantly steeper than the expected t^3 for a CNM transitioning from steep to flat at the Bondi radius. In order to explain the steeply rising gradient of the second radio flare observed, the CNM gradient would need to transition from $k \approx 2$ to 2.5 to $k \approx -0.5$ to -2.5 (i.e., an increase in the density with radius from the SMBH). In addition, if the second radio decay were due to CNM interactions, the CNM gradient would need to transition from positive to extremely steeply decaying ($k \approx 3$–5), to explain the rapid decay of the radio emission after the peak of the second flare. The steep rising light curves and unlikely values of k are therefore not consistent with the outflow encountering a transition in the CNM from steep to flat at the Bondi radius of the SMBH.

The sharp increase in the radio emission from AT2020vwl would require an extreme change in the density of the CNM. J. Zhuang et al. (2024) suggested that the interaction of TDE outflows encountering a molecular cloud in the central region of the galaxy may explain some late-time radio flares observed from TDEs. However, the increasing energy in the outflow observed during the second flare (Figure 5) is not explained by this scenario. The short duration of the second flare would require an interaction with a small dense molecular cloud, but the drastic increase in energy observed is not compatible with this scenario. We therefore find it unlikely that the rebrightening was triggered by a change in the density profile, or a localized densification, in the environment surrounding the outflow.

6.2. An Off-axis Relativistic Jet?

A late-time rise in the radio emission may be caused by an off-axis relativistic jet launched at or near the time of the stellar disruption. An off-axis jet naturally produces a steep rise in the observed radio light curve as the jet decelerates and spreads laterally, with a larger fraction of the jet coming into the observer's line of sight at late times (T. Matsumoto & T. Piran 2023). In the generalized equipartition model of T. Matsumoto & T. Piran (2023), the initially off-axis relativistic jet transitions to an on-axis Newtonian outflow at the time when the jet decelerates to subrelativistic velocities. The equipartition Newtonian velocity at this time must be $\beta_{\rm eq,N} > 0.23$, as for $\beta_{\rm eq,N}$ smaller than this, the minimal energies for on- and off-axis solutions have discrete branches, implying that extraordinarily high Γ values and an extremely off-axis jet would be required to explain the radio luminosity. T. Matsumoto & T. Piran (2023) give

$$\beta_{\rm Eq,N} \approx 0.73 \left[\frac{(F_p/{\rm mJy})^{8/17} (d_{\rm L}/10^{28}{\rm cm})^{16/17} \eta^{35/51}}{(\nu_p/10{\rm GHz})(1+z)^{8/17}} \right] \times \left(\frac{t}{100\ {\rm day}} \right)^{-1} f_A^{-7/17} f_V^{-1/17}, \quad (6)$$

where d_L is the luminosity distance and f_A and f_V are the geometric factors that describe the geometry of the outflow.

The peak flux density of the radio emission from AT2020vwl has been rising since the second flare began, with the final epoch at $t = 1220$ days having $F_p = 0.6 \pm 0.4$ mJy with $\nu_p = 0.8 \pm 0.4$ GHz. These values correspond to $\beta_{\rm Eq,N} = 0.03$ (assuming $f_A = f_V = 1$, as appropriate for a collimated jet), significantly lower than the required $\beta_{\rm Eq,N} = 0.23$ for an outflow at the transition from relativistic to Newtonian. We therefore find it unlikely that the second radio flare is due to an off-axis relativistic jet, as the observed outflow velocity at the time of the flare is too low for this scenario. If the peak flux were to continue to rise for an extended time period, the outflow may reach the critical transition velocity of $\beta_{\rm eq,N} = 0.23$. Although, given the observed flux density at frequencies >2 GHz has already begun decreasing, it is unlikely the peak flux density will continue to rise for sufficient time for this transition to occur.

In an alternative scenario, the transition from an off-axis to an on-axis jet may occur earlier, before the Newtonian phase. In this scenario, the radio emission observed should be in the relativistic regime. However, in order to obtain a relativistic solution to the evolution of the radio emission, the jet would have to be unphysically collimated (in order to obtain a self-consistent result where $\Gamma \sim 2$ requires $f_A < 0.01$, i.e., a jet with opening angle of $<0.1^\circ$). SMBH outflows are unlikely to produce a jet with such a small opening angle (e.g., S. G. Jorstad et al. 2005).

6.3. Renewed Energy Injection into the Outflow?

Increasing radio luminosity from a synchrotron-emitting outflow may be triggered by renewed energy injection into the outflow or the launching of a new outflow. For example, there are a handful of radio flares observed in GRB afterglows that have been attributed to energy injection (e.g., G. Schroeder et al. 2024), and in X-ray binaries, accretion disk state transitions are usually associated with radio jet launching (e.g., R. P. Fender et al. 2004). In the case of renewed energy injection episodes, rapid radio brightening can be triggered by rapid energy injection that dominates the energy of the initial blastwave (T. Laskar et al. 2015). For GRB afterglows with reflares attributed to energy injection, the optical and X-ray light curves usually also show a simultaneous rebrightening (T. Laskar et al. 2015). In the case of a TDE, prompt outflows are likely driven by debris interactions during the stellar disruption and circularization of the debris (e.g., W. Lu & C. Bonnerot 2020). Other outflows, by contrast, may be ejected in the form of an accretion-induced wind or jet once an accretion disk has formed (e.g., E. Ramirez-Ruiz & S. Rosswog 2009; S. van Velzen et al. 2011; K. D. Alexander et al. 2016) and may be delayed from the initial disruption, depending on the disk properties and accretion rate (F. De Colle et al. 2012). At least some TDEs produce highly relativistic jets at early times (e.g., SwiftJ1644 and AT2022cmc; J. S. Bloom et al. 2011; D. N. Burrows et al. 2011; A. J. Levan et al. 2011; B. A. Zauderer et al. 2011; I. Andreoni et al. 2022; D. R. Pasham et al. 2023), indicating that TDEs can provide the conditions for the launching of jets. It is currently unclear whether all TDEs produce jets (some less collimated than others) or if the conditions for jet launching are only reached occasionally in TDEs, although the deep observational limits of TDEs suggest powerful jets are rare (S. van Velzen et al. 2013).

State transitions of accretion disks in X-ray binaries are usually associated with changes in radio jet properties (R. P. Fender et al. 2004). In X-ray binaries in which stellar-mass black holes accrete at varying rates, steady, compact radio-emitting jets are observed during the "hard" accretion disk state, associated with flat or inverted radio spectra and X-ray corona emission in hard X-rays (see, e.g., R. P. Fender et al. 2004 for a review). Transient radio-emitting jets are usually launched during accretion disk state transitions to the "soft" accretion disk state, associated with bright, soft X-ray emission and optically thin radio outbursts (R. P. Fender et al. 2004). The transient jets associated with the outburst state are assumed to be more relativistic than the steady compact jets in the low state (R. P. Fender et al. 2004).

It is uncertain how similar TDE accretion disk properties and behaviors are to those of X-ray binaries. Evidence for accretion disk state transitions occurring in TDEs has been observed in a handful of events. T. Wevers et al. (2021) showed that the X-ray emission from AT2018fyk evolved from a blackbody to a power-law-dominated spectrum in less than 100 days. AT2021ehb gradually formed a dominant hard spectral component over 170 days, which softened dramatically within three days while the X-ray flux faded by an order of magnitude (Y. Yao et al. 2022). The partial TDE eRASSt J0456-20 also showed a dramatic softening in the X-ray spectrum while fading quickly (Z. Liu et al. 2023). At least some TDEs have the conditions required for a hot corona to form, as has been observed in the X-ray spectra of XMMSL1 0740–85 (R. D. Saxton et al. 2017) and AT2018fyk (T. Wevers et al. 2021). Additionally, J. T. Hinkle et al. (2024) and M. Newsome et al. (2024) discovered coronal line emission in a number of TDEs, giving tentative evidence of hot coronas in these sources. However, a strong link between X-ray accretion disk emission and the radio properties of TDEs has yet to be demonstrated.

The second radio flare observed from AT2020vwl resulted in an increase in flux density at all radio frequencies, with the emission peaking first at higher frequencies, similar to the first radio flare. However, the second radio flare rose significantly quicker than the first flare at all frequencies. Through modeling the radio light curves, we deduce that the first radio flare contributes very little flux density to the second flare at frequencies >1 GHz (Figure 2).

We investigate whether the sharp rise of $\nu L_\nu \propto t^4$ to t^7 for the second radio flare may be powered by an episode of energy injection. The duration of the flare is dependent on the duration of the energy injection, after which the outflow would continue to evolve as a blastwave but with increased kinetic energy (T. Laskar et al. 2015). In this scenario, we begin by noting that the light curves of synchrotron radiation from a nonrelativistic shock in the optically thin regime (above the spectral peak in this case, with $\nu_m < \nu_a < \nu < \nu_c$) depend on the total shock energy and time as $F_\nu \propto E^{0.8} t^{-2.4}$ for $p \approx 3$ and $k \approx 2.5$ (Appendix C). Assuming the energy rises as t^m during the injection phase, this implies a light-curve decline rate of $t^{0.8m-2.4}$. For the highest-frequency 11 GHz light curve (which is on the optically thin segment throughout and farthest from the spectral peak in our observations), we infer a rise rate of $a_2 = 7.2^{+2.0}_{-2.8}$ (Table 1), corresponding to an extremely steep energy injection rate of $m = 12^{+2.5}_{-3.5}$. This is marginally (2σ) consistent with the inferred energy increase rate from equipartition arguments, for which fitting the energy growth as a power law with time yields $m_{\rm eq} = 4.2 \pm 1.9$ (Table 4 and

Figure 5), making energy injection a possible explanation for the second radio flare. A. J. Goodwin et al. (2023) found that the first radio flare from AT2020vwl was well described by a single ejection of energy into an outflow at the onset of the stellar disruption, likely due to collisions between tidal debris streams. Energy injection into this outflow could take place if there is slower-moving outflow material traveling behind the main outflow that catches up with the forward shock when the latter decelerates (as seen in GRBs; e.g., R. Sari & P. Mészáros 2000; T. Laskar et al. 2015).

Alternatively, the chromatic evolution of the second radio flare, the increase in the peak frequency of the synchrotron spectrum, and the significant increase in the energy of the emitting region during the second flare could also be explained if the second flare is due to an entirely new outflow launched 160–700 days after the stellar disruption. In Section 5, we found evidence for a long-lived accretion disk in the optical and UV emission from the host galaxy of AT2020vwl. While there was no X-ray emission detected from the event at any point in its evolution, the X-ray upper limits allow a strong bound on the accretion rate to be obtained, under the assumption that the late-time X-ray emission is not obscured. We find that the disk is relatively low-mass ($\approx 0.01\ M_{\odot}$) and the accretion rate is significantly sub-Eddington ($\sim 0.1\ \dot{M}_{\rm Edd}$).

In summary, the second outflow carries significantly more energy than the first outflow and is potentially accelerating, perhaps indicating a new energy injection (Figure 5), strikingly different to the first radio flare observed. The form of this outflow is likely a mildly collimated jet launched at the time of the peak accretion rate in the disk (Figure 6), similar to transient radio jets that are launched during accretion episodes in X-ray binary systems. An accretion disk wind is also possible, but less likely as the accretion rate is significantly sub-Eddington and the second radio flare evolves quickly with increasing energy, different to the accretion-rate profile. Energy injection or the launch of a second outflow remain viable models for explaining the second flare.

6.4. Comparison to Other TDEs with Late-time Radio Flares

Late-time radio flares from TDEs are being discovered with increasing frequency. Y. Cendes et al. (2023) found that in a sample of 23 TDEs, ≈40% of events had detectable radio emission at late times. Some TDEs with early-time radio emission decay very slowly, over years (e.g., AT2019azh; A. J. Goodwin et al. 2022), while others decay more rapidly (e.g., ASASSN-14li; K. D. Alexander et al. 2016). Of the TDEs that have shown late-time (>500 days) rising radio emission, only ASASSN-15oi and AT2019dsg have constraining radio observations at early times (Y. Cendes et al. 2021; A. Horesh et al. 2021a; R. Stein et al. 2021; A. Hajela et al. 2024). Interestingly, most late-time radio flares observed from TDEs are consistent with a second outflow launched hundreds of days after the stellar disruption (Y. Cendes et al. 2023). A comparison between the radio light curve of AT2020vwl and TDEs with well-sampled late-time radio flares is shown in Figure 7.

Two distinct radio emission episodes have been discovered in the TDE ASASSN-15oi (A. Horesh et al. 2021a; A. Hajela et al. 2024) and suggested for the TDE ASASSN-19bt (C. T. Christy et al. 2024). A. Hajela et al. (2024) found that for ASASSN-15oi, the first radio flare rose as $F_{\nu} \propto t^{4.5}$ and decayed as $F_{\nu} \propto t^{-1}$, while the second flare rose with $F_{\nu} \propto t^{4}$ and decayed as $F_{\nu} \propto t^{-1.5}$

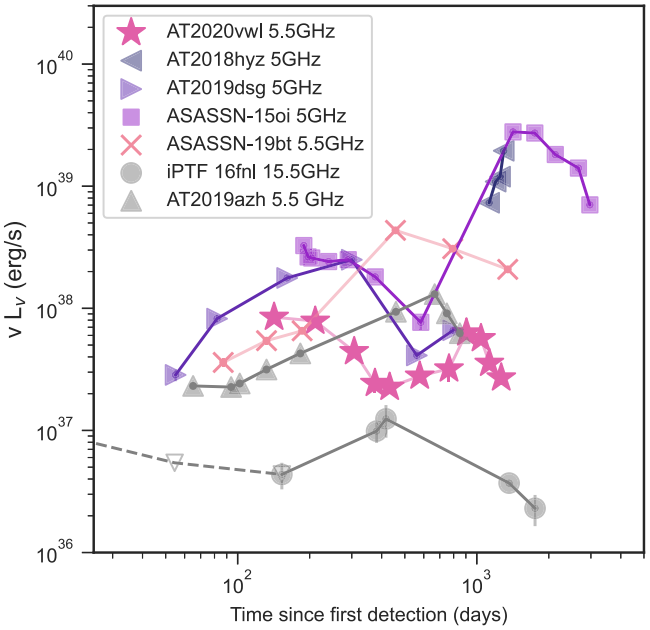

Figure 7. Radio light curves of TDEs suggested to have late-rising radio emission or two radio light-curve components. The TDEs shown in gray are consistent with a single outflow ejection and no late-time radio flare. The second radio flare observed from AT2020vwl rises and decays much faster than most other late radio flares observed. The radio data are from Y. Cendes et al. (2022; AT2018hyz), C. T. Christy et al. (2024; ASASSN-19bt), A. Horesh et al. (2021a), A. Hajela et al. (2024; ASASSN-15oi), Y. Cendes et al. (2021, 2023; AT2019dsg), A. Horesh et al. (2021b; iPTF16fnl), and A. J. Goodwin et al. (2022; AT2019azh). The empty triangles represent 3σ upper limits.

until 2660 days, at which time the decay steepened to $F_{\nu} \propto t^{-7}$. The rise and decay rates of the first flare from AT2020vwl are similar (within uncertainties) of the first flare from ASASSN-15oi. AT2020vwl's second flare, however, rose and decayed slightly more quickly than ASASSN-15oi. Similar to AT2020vwl, the first radio flare from ASASSN-15oi is very well explained by a collision-induced outflow, in which material is ejected via stream–stream collisions of the stellar debris during the circularization process (W. Lu & C. Bonnerot 2020; A. Hajela et al. 2024). As for AT2020vwl, A. Hajela et al. (2024) found that the outflow that powers the second radio flare seen from ASASSN-15oi carries substantially more energy than the first flare, and they propose that the second radio flare is powered by a second outflow launched around the time of peak accretion at ≈200 days post optical flare. Unlike AT2020vwl, ASASSN-15oi was detected in X-rays, motivating the suggestion that the second radio flare is powered by an accretion-induced wind or mildly collimated jet.

AT2018hyz has shown perhaps the most extreme late-time flare, with the radio luminosity increasing as $L \propto t^{5}$ at times >1000 days post optical flare (Y. Cendes et al. 2022). Y. Cendes et al. (2022) modeled the radio spectra of this source and deduced the emission was consistent with a mildly collimated delayed jet that was launched ≈450 days post optical flare. I. Sfaradi et al. (2024) proposed that the radio emission from AT2018hyz can be explained by an off-axis prompt relativistic jet launched at the time of the optical flare. Regardless of the mechanism behind the late-rising radio emission from AT2018hyz, the evolution of the radio emission is quite different to the late-time flare from AT2020vwl. The intrinsic luminosity of the radio emission from AT2018hyz is approximately an order of magnitude higher than that of AT2020vwl, and the inferred velocity of the radio-emitting

region of the former is significantly higher ($>0.25\,c$ compared to $\approx 0.03c$). The late radio flare from AT2018hyz showed no sign of beginning to decay at 5 GHz at 1300 days post disruption, whereas the second flare of AT2020vwl rose for ≈500 days, to peak around 1000 days post disruption, before decaying again. If the late-time radio emission from AT2018hyz and AT2020vwl is explained by the same mechanism, it is clear the outflow in AT2020vwl is significantly slower, less energetic, and shorter-lived than that of AT2018hyz. These differences may be caused by a larger accretion disk in AT2018hyz that is able to launch a stronger jet than that of AT2020vwl.

A. Horesh et al. (2021b) reported a potential late-time radio flare from iPTF16fnl; however, due to the intrinsically low luminosity of the radio emission from this source, in Figure 7 it is clear that it is consistent with a faint single flare that started around the time of the initial stellar disruption. I. Sfaradi et al. (2022) reported a possible late-time flare in the TDE AT2019azh, but when taking into consideration the full long-term radio light curve presented in A. J. Goodwin et al. (2022) it is evident that the light-curve evolution is consistent with small amplitude fluctuations in the overall slow rise and decay of the radio emission of this TDE.

7. Summary

Our long-term radio observations of the TDE AT2020vwl reveal a second radio flare, beginning at approximately 400 days post optical flare. The second radio flare rose and decayed quickly at frequencies >2 GHz, unlike late-time flares observed from other TDEs.

We find the second radio flare from AT2020vwl is unlikely to be due to changes in the circumnuclear density distribution or an off-axis jet. We propose that the second radio flare is instead due to either a period of new energy injection into the preexisting outflow or a second outflow, launched hundreds of days post stellar disruption and coincident with the peak accretion rate of the accretion disk that is implied by the optical and UV plateaus in the respective light curves.

There is mounting evidence that TDEs launch multiple types of outflows, with prompt radio-emitting outflows being well explained by outflows ejected by debris stream collisions, while delayed outflows may be launched by the accretion disk, which can exist for years after the TDE. ASASSN-15oi and AT2020vwl are the only two TDEs to date that have both prompt and late-type outflows observed in the radio, due to continuous radio coverage over many years after discovery. Future observations that track the long-term evolution of the radio emission from TDEs and search for any relationship between long-lived accretion disks and delayed radio flares will be crucial in confirming the launching of multiple types of radio outflows in TDEs.

Acknowledgments

A.G. is grateful for support from the Forrest Research Foundation. This work was supported by the Australian government through the Australian Research Council's Discovery Projects funding scheme (DP200102471). This research was supported in part by the National Science Foundation under PHY-1748958. K.D.A. and C.C. acknowledge the support provided by the NSF through award AST-2307668. C.C. additionally acknowledges NSF and NRAO support from award SOSPA9-007. This research benefited from interactions that were funded by the Gordon and Betty Moore Foundation through grant GBMF5076. The National Radio Astronomy Observatory is a facility of the National Science Foundation operated under cooperative agreement by Associated Universities, Inc. We thank the staff of the GMRT that made these observations possible. GMRT is run by the National Center for Radio Astrophysics of the Tata Institute of Fundamental Research. The MeerKAT telescope is operated by the South African Radio Astronomy Observatory, which is a facility of the National Research Foundation, an agency of the Department of Science and Innovation.

Facilities: VLA, MeerKAT, GMRT, Swift (XRT and UVOT).

Appendix A
Radio Observations

A summary of the radio observations of AT2020vwl is shown in Table 3.

Table 3
New Radio Observations of AT2020vwl

Date (UTC)	Instrument and Configuration	Proposal ID	Frequency (GHz)	Flux Density ± Statistical Error ± ISS Error (μJy)
2022-11-01	VLA-C	20B-377	1.5	186 ± 89 ± 74
			2.77	311 ± 35 ± 62
			3.24	366 ± 25 ± 73
			4.48	216 ± 39 ± 17
			5.51	205 ± 45 ± 16
			6.59	127 ± 28 ± 10
			7.45	82 ± 32 ± 2
			9.1	82 ± 11 ± 2
			11.12	74 ± 16 ± 2
			13.55	56 ± 9 ± 1
			16.61	29 ± 9 ± 1
2023-02-01	GMRT	43_046	0.65	292 ± 42 ± 58
2023-02-01	GMRT	43_046	1.26	417 ± 41 ± 167
2023-04-22	GMRT	44_022	0.65	156 ± 54 ± 31
2023-04-01	VLA-B	23A-202	1.263	604 ± 53 ± 242
			1.65	471 ± 95 ± 188

Table 3
(Continued)

Date (UTC)	Instrument and Configuration	Proposal ID	Frequency (GHz)	Flux Density ± Statistical Error ± ISS Error (μJy)
			1.9	742 ± 43 ± 297
			2.24	699 ± 44 ± 140
			2.75	639 ± 21 ± 128
			3.25	578 ± 18 ± 116
			3.75	562 ± 17 ± 112
			4.49	488 ± 23 ± 39
			5.51	404 ± 22 ± 32
			6.49	414 ± 24 ± 33
			9.0	325 ± 14 ± 7
			11.0	274 ± 13 ± 6
2023-08-31	GMRT	44_022	0.65	689 ± 59 ± 138
2023-08-31	GMRT	44_022	1.26	601 ± 64 ± 240
2023-08-01	VLA-A	23A-202	1.14	692 ± 148 ± 277
			1.4	639 ± 39 ± 256
			1.65	598 ± 71 ± 239
			1.9	590 ± 31 ± 236
			2.24	696 ± 43 ± 139
			2.75	689 ± 26 ± 138
			3.25	625 ± 21 ± 125
			3.75	549 ± 19 ± 110
			4.49	512 ± 26 ± 41
			5.51	363 ± 28 ± 29
			6.49	338 ± 28 ± 27
			7.51	283 ± 26 ± 6
			9.0	188 ± 16 ± 4
			11.0	189 ± 37 ± 4
2023-11-15	GMRT	45_123	0.65	595 ± 93 ± 119
2023-11-10	VLA-D	23B-078	2.75	425 ± 39 ± 85
			3.24	434 ± 32 ± 87
			3.75	441 ± 103 ± 88
			4.49	298 ± 41 ± 24
			5.51	228 ± 22 ± 18
			6.49	210 ± 25 ± 17
			7.51	180 ± 24 ± 4
			9.0	133 ± 17 ± 3
			11.0	89 ± 21 ± 2
2024-02-27	MeerKAT	SCI-20230907-AG-01	0.82	1131 ± 45 ± 226
2024-03-26	VLA-C	24A-159	2.24	568 ± 77 ± 114
			2.75	366 ± 35 ± 73
			4.5	201 ± 26 ± 16
			5.5	173 ± 21 ± 14
			6.49	178 ± 19 ± 14
			7.51	111 ± 18 ± 2
			9.0	106 ± 14 ± 2
			11.0	79 ± 16 ± 2
			13.5	60 ± 9 ± 1
			16.62	47 ± 10 ± 1

(This table is available in its entirety in machine-readable form in the online article.)

Appendix B
Spectral Fitting Parameters and Outflow Constraints

The spectral fitting and outflow model parameters fitted in Section 4 are given in Table 4.

Table 4
Modeled Radio Spectra and Outflow Properties for AT2020vwl

Date (UTC)	δt[a] (day)	F_p (mJy)	ν_m (GHz)	ν_p (GHz)	p	log E (erg)	log R (cm)	β (c)	log n_e (cm^{-3})	log B (G)	log M_{ej} ($M_\odot$)
Spherical Geometry											
27/2/2021	142	0.59 ± 0.04	4.02 ± 1.09	7.44 ± 0.63	2.91 ± 0.27	48.07 ± 0.07	16.11 ± 0.06	0.035 ± 0.005	3.80 ± 0.55	−0.14 ± 0.41	−2.98 ± 0.10
7/5/2021	211	0.53 ± 0.04	3.06 ± 0.90	5.74 ± 0.66	2.92 ± 0.26	48.13 ± 0.08	16.21 ± 0.07	0.029 ± 0.005	3.59 ± 0.59	−0.24 ± 0.45	−2.76 ± 0.11
11/8/2021	307	0.37 ± 0.07	1.47 ± 0.52	2.75 ± 0.47	3.02 ± 0.22	48.35 ± 0.13	16.46 ± 0.09	0.036 ± 0.008	3.05 ± 0.81	−0.52 ± 0.58	−2.72 ± 0.16
18/10/2021	375	0.23 ± 0.14	1.19 ± 0.59	2.25 ± 0.65	3.05 ± 0.22	48.21 ± 0.35	16.45 ± 0.17	0.029 ± 0.012	2.94 ± 1.57	−0.57 ± 1.04	−2.67 ± 0.39
14/12/2021	432	0.14 ± 0.04	1.43 ± 0.72	2.75 ± 0.84	2.97 ± 0.26	47.79 ± 0.20	16.26 ± 0.13	0.016 ± 0.005	3.11 ± 1.13	−0.49 ± 0.82	−2.59 ± 0.24
8/5/2022	577	0.27 ± 0.09	0.81 ± 0.36	1.55 ± 0.41	3.08 ± 0.21	48.48 ± 0.20	16.65 ± 0.12	0.030 ± 0.008	2.62 ± 1.10	−0.73 ± 0.76	−2.42 ± 0.24
1/11/2022	765	0.16 ± 0.07	⋯	2.20 ± 0.66	3.09 ± 0.21	48.05 ± 0.27	16.39 ± 0.15	0.013 ± 0.004	2.98 ± 1.39	−0.55 ± 0.94	−2.10 ± 0.31
1/4/2023	905	0.48 ± 0.06	⋯	3.55 ± 0.40	2.90 ± 0.26	48.27 ± 0.12	16.39 ± 0.10	0.011 ± 0.003	3.17 ± 0.87	−0.45 ± 0.66	−1.75 ± 0.16
1/8/2023	1041	0.56 ± 0.08	⋯	2.05 ± 0.27	3.09 ± 0.20	48.75 ± 0.13	16.68 ± 0.11	0.018 ± 0.004	2.80 ± 0.95	−0.64 ± 0.69	−1.71 ± 0.17
10/11/2023	1128	0.31 ± 0.08	⋯	2.15 ± 0.53	3.04 ± 0.23	48.37 ± 0.18	16.53 ± 0.13	0.012 ± 0.003	2.87 ± 1.11	−0.61 ± 0.80	−1.73 ± 0.22
26/3/2024	1265	0.53 ± 0.23	⋯	0.85 ± 0.31	3.11 ± 0.18	49.12 ± 0.26	17.05 ± 0.16	0.034 ± 0.012	2.06 ± 1.41	−1.02 ± 0.97	−1.90 ± 0.30
Conical Geometry											
	142					48.59 ± 0.07	16.49 ± 0.06	0.080 ± 0.012	3.27 ± 0.55	−0.41 ± 0.41	−3.16 ± 0.10
	211					48.66 ± 0.08	16.58 ± 0.07	0.067 ± 0.011	3.06 ± 0.59	−0.51 ± 0.45	−2.95 ± 0.11
	307					48.89 ± 0.13	16.84 ± 0.09	0.082 ± 0.017	2.52 ± 0.81	−0.78 ± 0.58	−2.89 ± 0.16
	375					48.75 ± 0.35	16.83 ± 0.17	0.067 ± 0.026	2.41 ± 1.57	−0.84 ± 1.04	−2.85 ± 0.39
	432					48.32 ± 0.20	16.63 ± 0.13	0.038 ± 0.011	2.57 ± 1.13	−0.75 ± 0.82	−2.79 ± 0.24
	577					49.02 ± 0.20	17.03 ± 0.12	0.068 ± 0.019	2.09 ± 1.10	−1.00 ± 0.76	−2.60 ± 0.24
	765					48.59 ± 0.27	16.76 ± 0.15	0.029 ± 0.010	2.45 ± 1.39	−0.82 ± 0.94	−2.30 ± 0.31
	905					48.80 ± 0.12	16.77 ± 0.10	0.025 ± 0.006	2.63 ± 0.87	−0.72 ± 0.66	−1.96 ± 0.16
	1041					49.29 ± 0.13	17.05 ± 0.11	0.042 ± 0.010	2.27 ± 0.95	−0.91 ± 0.69	−1.90 ± 0.17
	1128					48.91 ± 0.18	16.91 ± 0.13	0.028 ± 0.008	2.33 ± 1.11	−0.87 ± 0.80	−1.93 ± 0.22
	1265					49.66 ± 0.26	17.43 ± 0.16	0.078 ± 0.028	1.53 ± 1.41	−1.28 ± 0.97	−2.08 ± 0.30

Note. The observations between 97 and 532 days post optical flare were published in A. J. Goodwin et al. (2023).
[a] δt is measured with respect to the beginning of the optical flare, MJD 59130.

Appendix C
Optically Thin Synchrotron Emission from Nonrelativistic Outflows in Stratified Media

Consider a point explosion of energy, E, driving a nonrelativistic shock with speed $\beta_{\rm sh} = \dot{r}_{\rm sh}/c$ into a stratified medium with density structure $\rho \propto r^{-k}$. The shock speed and radius as a function of time are given by the Sedov–Taylor–von Neumann solution, with $r_{\rm sh} \propto E^{\frac{1}{5-k}} t^{\frac{2}{5-k}}$ and $\beta_{\rm sh} \propto E^{\frac{1}{5-k}} t^{-\frac{3}{5-k}}$, such that $\rho r^3 \beta_{\rm sh}^2 = {\rm const}$. We assume that a fixed fraction of the internal energy density of the postshock fluid is given to magnetic fields ($B^2 \propto \epsilon_{\rm B} \rho \beta_{\rm sh}^2$), such that

$$B \propto \rho^{\frac{1}{2}} \beta_{\rm sh} \propto E^{\frac{2-k}{2(5-k)}} t^{-\frac{3}{5-k}}. \tag{C1}$$

The characteristic synchrotron frequency for electrons with Lorentz factor γ_e moving at angle α in a magnetic field B (in SI units) is given by

$$\nu \sim \frac{1}{1+z} \frac{3}{4\pi} \gamma_e^2 \frac{eB}{m_e} \sin\alpha \propto \gamma_e^2 B. \tag{C2}$$

This implies that the Lorentz factor of electrons that dominate the emission at an observing frequency ν is given by

$$\gamma_e \propto \nu^{1/2} B^{-1/2} \propto \nu^{1/2} E^{-\frac{2-k}{4(5-k)}} t^{\frac{3}{2(5-k)}}. \tag{C3}$$

Since the radiation emitted by these electrons peaks at P_ν, such that $\nu P_\nu \sim P_{\rm syn} \propto \gamma_e^2 B^2$ is the synchrotron energy loss rate, the specific power,

$$P_\nu \propto \frac{P_{\rm syn}}{\nu} \propto B \propto E^{\frac{2-k}{2(5-k)}} t^{-\frac{3}{5-k}}, \tag{C4}$$

is independent of γ_e.

We assume that the shock accelerates electrons into a power-law distribution in the electron Lorentz factor γ_e, such that $dN_e/d\gamma_e \propto \gamma^{-p}$ above a minimum Lorentz factor γ_m. The standard assumption that electrons at $\gamma_e > \gamma_m$ carry a fraction ϵ_e of the shock energy leads to $\gamma_m \approx \epsilon_e \frac{\beta_{\rm sh}^2}{2} \frac{m_p}{m_e}$ for nonrelativistic shocks. For values of $\epsilon_e \lesssim 0.1$, this expression breaks down when $\beta_{\rm sh} \lesssim 0.1$. In this regime, it is important to include the deviation of the electron participation fraction from unity (D. Eichler & E. Waxman 2005; L. Sironi & D. Giannios 2013). Following L. Sironi & D. Giannios (2013), we have

$$\gamma_m = \max[1, x], f_{\rm NT} = \min[1, x, x^{p-1/2}], x \equiv \epsilon_e \frac{\beta_{\rm sh}^2}{2} \frac{m_p}{m_e}, \tag{C5}$$

where $f_{\rm NT}$ is the fraction of particles accelerated into the nonthermal distribution. For $\epsilon_e \beta_{\rm sh}^2 \lesssim 2 m_e/m_p \approx \times 10^{-3}$, we have $x < 1$, $\gamma_m \sim 1$, and $f_{\rm NT} = \min[x, x^{(p-1)/2}]$. This leads to the following choices for $f_{\rm NT}$:

$$f_{\rm NT} = \begin{cases} x^{(p-1)/2} \propto \beta_{\rm sh}^{p-1}, & p \gtrsim 3 \\ x \propto \beta_{\rm sh}^2, & 2 < p < 3 \end{cases}. \tag{C6}$$

The specific luminosity above the synchrotron self-absorption break is then given by the product of the number of electrons emitting near the frequency ν and the specific power per electron,

$$L_\nu = N_e \nu P_\nu \propto f_{\rm NT} N_e (\gamma_e/\gamma_m)^{1-p} P_\nu, \tag{C7}$$

where

$$N_e \propto \rho r_{\rm sh}^3 \propto r^{3-k} \tag{C8}$$

is the total number of electrons swept up by the shock. Taking $\gamma_m \sim 1$ and substituting the expression for $f_{\rm NT}$ from Equation (C6), along with γ_e from Equation (C3), and P_ν from Equation (C4) into Equation (C7), the observed luminosity in the optically thin regime is given by

$$L_\nu \propto \begin{cases} \nu^{\frac{1-p}{2}} E^{\frac{(p-1)(6-k)+(16-6k)}{4(5-k)}} t^{-\frac{2(3-k)(p-3)+3(p+1)}{2(5-k)}}, & p \gtrsim 3 \\ \nu^{\frac{1-p}{2}} E^{\frac{6(4-k)+(k-2)(1-p)}{4(5-k)}} t^{-\frac{3(p+1)}{2(5-k)}}, & 2 < p < 3. \end{cases} \tag{C9}$$

These give the consistent solution $L_\nu \propto E^{\frac{7-2k}{5-k}} t^{-\frac{6}{5-k}}$ for $p = 3$. In addition, for the typical values of $k \approx 2.5$ inferred for radio TDEs, this suggests that the optically thin synchrotron spectrum $L_\nu \propto E^{0.8} t^{-2.4}$ for $p \approx 3$.

ORCID iDs

A. J. Goodwin https://orcid.org/0000-0003-3441-8299
T. Laskar https://orcid.org/0000-0003-1792-2338
K. D. Alexander https://orcid.org/0000-0002-8297-2473
G. E. Anderson https://orcid.org/0000-0001-6544-8007
C. T. Christy https://orcid.org/0000-0003-0528-202X
R. Margutti https://orcid.org/0000-0003-4768-7586
S. van Velzen https://orcid.org/0000-0002-3859-8074

References

Alexander, K. D., Berger, E., Guillochon, J., Zauderer, B. A., & Williams, P. K. G. 2016, ApJL, 819, L25
Alexander, K. D., van Velzen, S., Horesh, A., & Zauderer, B. A. 2020, SSRv, 216, 81
Anderson, G. E., Horesh, A., Mooley, K. P., et al. 2017, MNRAS, 466, 3648
Andreoni, I., Coughlin, M. W., Perley, D. A., et al. 2022, Natur, 612, 430
Anumarlapudi, A., Dobie, D., Kaplan, D. L., et al. 2024, ApJ, 974, 241
Auchettl, K., Guillochon, J., & Ramirez-Ruiz, E. 2017, ApJ, 838, 149
Balbus, S. A. 2017, MNRAS, 471, 4832
Barniol Duran, R., Nakar, E., & Piran, T. 2013, ApJ, 772, 78
Bloom, J. S., Giannios, D., Metzger, B. D., et al. 2011, Sci, 333, 203
Bonnerot, C., Rossi, E. M., Lodato, G., & Price, D. J. 2016, MNRAS, 455, 2253
Burrows, D. N., Kennea, J. A., Ghisellini, G., et al. 2011, Natur, 476, 421
CASA Team, Bean, B., Bhatnagar, S., et al. 2022, PASP, 134, 114501
Cendes, Y., Alexander, K. D., Berger, E., et al. 2021, ApJ, 919, 127
Cendes, Y., Berger, E., Alexander, K. D., et al. 2022, ApJ, 938, 28
Cendes, Y., Berger, E., Alexander, K. D., et al. 2023, ApJ, 971, 185
Chevalier, R. A. 1998, ApJ, 499, 810
Christy, C. T., Alexander, K. D., Cendes, Y., et al. 2024, ApJ, 974, 18
Dai, L., McKinney, J. C., & Miller, M. C. 2015, ApJL, 812, L39
De Colle, F., Guillochon, J., Naiman, J., & Ramirez-Ruiz, E. 2012, ApJ, 760, 103
Eichler, D., & Waxman, E. 2005, ApJ, 627, 861
Evans, P. A., Beardmore, A. P., Page, K. L., et al. 2009, MNRAS, 397, 1177
Fender, R. P., Belloni, T. M., & Gallo, E. 2004, MNRAS, 355, 1105
Foreman-Mackey, D., Hogg, D. W., Lang, D., & Goodman, J. 2013, PASP, 125, 306
Gehrels, N., Chincarini, G., Giommi, P., et al. 2004, ApJ, 611, 1005
Gezari, S., Heckman, T., Cenko, S. B., et al. 2009, ApJ, 698, 1367
Goodwin, A. J., Alexander, K. D., Miller-Jones, J. C. A., et al. 2023, MNRAS, 522, 5084
Goodwin, A. J., Anderson, G. E., Miller-Jones, J. C. A., et al. 2024, MNRAS, 528, 7123
Goodwin, A. J., van Velzen, S., Miller-Jones, J. C. A., et al. 2022, MNRAS, 511, 5328
Granot, J., & Sari, R. 2002, ApJ, 568, 820
Guillochon, J., Manukian, H., & Ramirez-Ruiz, E. 2014, ApJ, 783, 23
Guolo, M., Gezari, S., Yao, Y., et al. 2024, ApJ, 966, 160

Hajela, A., Alexander, K. D., Margutti, R., et al. 2024, arXiv:2407.19019
Hammerstein, E., Gezari, S., Velzen, S. V., et al. 2021, TNSCR, 1, 2021–955
Hammerstein, E., van Velzen, S., Gezari, S., et al. 2023, ApJ, 942, 9
Hayasaki, K., Stone, N., & Loeb, A. 2016, MNRAS, 461, 3760
Hinkle, J. T., Shappee, B. J., & Holoien, T. W. S. 2024, MNRAS, 528, 4775
Heywood, I., 2020 oxkat: Semi-automated imaging of MeerKAT observations, Astrophysics Source Code Library, ascl:2009.003
Hodgkin, S. T., Breedt, E., Delgado, A., et al. 2020, TNSTR, 1, 2020–3
Horesh, A., Cenko, S. B., & Arcavi, I. 2021a, NatAs, 5, 491
Horesh, A., Sfaradi, I., Fender, R., et al. 2021b, ApJL, 920, L5
Jorstad, S. G., Marscher, A. P., Lister, M. L., et al. 2005, AJ, 130, 1418
Krolik, J., Piran, T., Svirski, G., & Cheng, R. M. 2016, ApJ, 827, 127
Laskar, T., Berger, E., Margutti, R., et al. 2015, ApJ, 814, 1
Levan, A. J., Tanvir, N. R., Cenko, S. B., et al. 2011, Sci, 333, 199
Liu, Z., Malyali, A., Krumpe, M., et al. 2023, A&A, 669, A75
Liu, Z., Ryu, T., Goodwin, A. J., et al. 2024, A&A, 683, L13
Loeb, A., & Ulmer, A. 1997, ApJ, 489, 573
Lu, W., & Bonnerot, C. 2020, MNRAS, 492, 686
Malyali, A., Liu, Z., Rau, A., et al. 2023, MNRAS, 520, 3549
Malyali, A., Rau, A., Bonnerot, C., et al. 2024, MNRAS, 531, 1256
Matsumoto, T., & Piran, T. 2023, MNRAS, 522, 4565
Matsumoto, T., & Piran, T. 2024, ApJ, 971, 49
McMullin, J. P., Waters, B., Schiebel, D., Young, W., & Golap, K. 2007, in ASP Conf. Ser. 376, Astronomical Data Analysis Software and Systems XVI, ed. R. A. Shaw, F. Hill, & D. J. Bell (San Francisco, CA: ASP), 127
Metzger, B. D. 2022, ApJL, 937, L12
Metzger, B. D., & Stone, N. C. 2016, MNRAS, 461, 948
Mockler, B., Guillochon, J., & Ramirez-Ruiz, E. 2019, ApJ, 872, 151
Mummery, A. 2023, MNRAS, 518, 1905
Mummery, A., & Balbus, S. A. 2020, MNRAS, 492, 5655
Mummery, A., Nathan, E., Ingram, A., & Gardner, M., 2024a FitTeD: Fitting Transients with Discs, Astrophysics Source Code Library, ascl:2412.019
Mummery, A., van Velzen, S., Nathan, E., et al. 2024b, MNRAS, 527, 2452
Newsome, M., Arcavi, I., Howell, D. A., et al. 2024, ApJ, 977, 258
Nicholl, M., Wevers, T., Oates, S. R., et al. 2020, MNRAS, 499, 482
Pasham, D. R., Lucchini, M., Laskar, T., et al. 2023, NatAs, 7, 88
Phinney, E. S. 1989, in IAU Symp. 136, The Center of the Galaxy, ed. M. Morris (Dordrecht: Kluwer), 543
Ramirez-Ruiz, E., & Rosswog, S. 2009, ApJL, 697, L77
Rees, M. J. 1988, Natur, 333, 523
Roth, N., Kasen, D., Guillochon, J., & Ramirez-Ruiz, E. 2016, ApJ, 827, 3
Salas, P., Bauer, F. E., Stockdale, C., & Prieto, J. L. 2013, MNRAS, 428, 1207
Sari, R., & Mészáros, P. 2000, ApJL, 535, L33
Saxton, R. D., Read, A. M., Komossa, S., et al. 2017, A&A, 598, A29
Schroeder, G., Rhodes, L., Laskar, T., et al. 2024, ApJ, 970, 139
Sfaradi, I., Beniamini, P., Horesh, A., et al. 2024, MNRAS, 527, 7672
Sfaradi, I., Horesh, A., Fender, R., et al. 2022, ApJ, 933, 176
Shiokawa, H., Krolik, J. H., Cheng, R. M., Piran, T., & Noble, S. C. 2015, ApJ, 804, 85
Sironi, L., & Giannios, D. 2013, ApJ, 778, 107
Somalwar, J. J., Ravi, V., Yao, Y., et al. 2023, arXiv:2310.03782
Stein, R., Velzen, S., Kowalski, M., et al. 2021, NatAs, 5, 510
Stroh, M. C., Terreran, G., Coppejans, D. L., et al. 2021, ApJL, 923, L24
Thomsen, L. L., Kwan, T. M., Dai, L., et al. 2022, ApJL, 937, L28
van Velzen, S., Anderson, G. E., Stone, N. C., et al. 2016, Sci, 351, 62
van Velzen, S., Frail, D. A., Körding, E., & Falcke, H. 2013, A&A, 552, A5
van Velzen, S., Gezari, S., Hammerstein, E., et al. 2021, ApJ, 908, 4
van Velzen, S., Holoien, T. W. S., Onori, F., Hung, T., & Arcavi, I. 2020, SSRv, 216, 124
van Velzen, S., Körding, E., & Falcke, H. 2011, MNRAS, 417, L51
Walker, M. A. 1998, MNRAS, 294, 307
Wevers, T., Pasham, D. R., van Velzen, S., et al. 2021, ApJ, 912, 151
Willingale, R., Starling, R. L. C., Beardmore, A. P., Tanvir, N. R., & O'Brien, P. T. 2013, MNRAS, 431, 394
Yao, Y., Lu, W., Guolo, M., et al. 2022, ApJ, 937, 8
Yao, Y., Ravi, V., Gezari, S., et al. 2023, ApJL, 955, L6
Zauderer, B. A., Berger, E., Soderberg, A. M., et al. 2011, Natur, 476, 425
Zhuang, J., Shen, R.-F., Mou, G., & Lu, W. 2024, arXiv:2406.08012